Journal of Physics and Chemistry of Solids 172 (2023) 111089

Contents lists available at ScienceDirect

Journal of Physics and Chemistry of Solids

journal homepage: www.elsevier.com/locate/jpcs

Carboxyl and thiol-functionalized magnetic nanoadsorbents for efficient and simultaneous removal of Pb(II), Cd(II), and Ni(II) heavy metal ions from aqueous solutions: Studies of adsorption, kinetics, and isotherms

V.P. Kothavale [a,b], A. Sharma [c], R.P. Dhavale [d], V.D. Chavan [e], S.R. Shingte [a], O. Selyshchev [c], T.D. Dongale [e], H.H. Park [d], D.R.T. Zahn [c], G. Salvan [c], P.B. Patil [a,*]

[a] Department of Physics, The New College, Shivaji University, Kolhapur, Maharashtra, 416012, India
[b] Department of Physics, Bhogawati Mahavidyalaya, Kurukali, Shivaji University, Kolhapur, Maharashtra, 416012, India
[c] Semiconductor Physics, Chemnitz University of Technology, 09107, Chemnitz, Germany
[d] Department of Materials Science and Engineering, Yonsei University, 50 Yonsei-ro, Seodaemun-gu, Seoul, 03722, South Korea
[e] School of Nanoscience and Technology, Shivaji University Kolhapur, Maharashtra, 416004, India

ARTICLE INFO

Keywords:
MNPs
Magnetic nanoparticles
Heavy metal ions (HMIs) removal
Ligand exchange
Adsorption
Simultaneous removal

ABSTRACT

Magnetic nanoparticles (MNPs) are important adsorbents for removing heavy metal ions (HMIs) from water due to their high surface area, abundant active adsorption sites after functionalization, magnetic separability, and reusability. However, compared with removing a single type of metal ion (single system), the simultaneous removal of multiple coexisting types of HMIs (e.g., ternary system) is challenging. To address this issue, in this study, Fe_3O_4 MNPs were functionalized with thiol (–SH) and carboxylic (–COOH) groups using meso-2,3-dimercaptosuccinic acid (DMSA). The MNP-DMSA nanoadsorbent was used for the simultaneous removal of Pb(II), Ni(II), and Cd(II) from aqueous solutions. The nanoadsorbent was extensively characterized and its adsorption behavior was investigated based on kinetic and isotherm studies using batch adsorption experiments. Highly monodispersed MNPs with the size of 8.24 ± 1 nm and the pure magnetite phase were synthesized using the thermal decomposition method. Fourier transform infrared spectroscopy and X-ray photoelectron spectroscopy analyses confirmed the successful modification of the surfaces of the MNPs by DMSA ligands. The MNP-DMSA nanoadsorbents exhibited good colloidal stability according to zeta potential measurements. The maximum adsorption capacities (q_m) for the simultaneous removal of Pb(II), Ni(II), and Cd(II) in the ternary system were determined as 64.5, 53.9, and 27.18 mg/g, respectively. In single systems, the q_m values for Pb(II), Ni(II), and Cd(II) were increased to 116.54, 102.73, and 75.48 mg/g, respectively. The adsorption kinetics and isotherm followed Langmuir and pseudo-second order models, respectively. An adsorption/desorption experiment demonstrated the reusability of the nanoadsorbent.

1. Introduction

The tremendous increase in the contamination of water streams with heavy metal ion (HMI) has been observed during recent decades. The primary source of these contaminants is industrial waste generated by the textile, pesticide, fertilizer, metal plating, tanneries, leather, mining, and paint production industries [1,2]. These HMIs are non-biodegradable and hazardous to living systems [3,4]. Several methods have been utilized for removing HMIs from effluents, such as membrane filtration, coagulation, microbial systems, electrochemical processes, and adsorption [5,6]. In particular, adsorption is advantageous due to its low cost and high efficiency [7,8]. Various adsorbents have been explored such as clay minerals [9], activated carbon [10], zeolite [11], silica gel [12], and magnetic nanoparticles (MNPs) [13]. MNPs exhibit good adsorption performance due to their high specific surface area, good colloidal stability, and short equilibrium time. Furthermore, MNPs can be separated from wastewater using an external magnet. Thus, the synergistic combination of efficient adsorption and magnetic separation is advantageous for removing HMIs from water using MNPs [14,15].

To improve their adsorption capacity (q_e), the surfaces of MNPs need to be functionalized using organic or inorganic materials to provide

* Corresponding author.
E-mail address: prashantphy@gmail.com (P.B. Patil).

https://doi.org/10.1016/j.jpcs.2022.111089
Received 4 December 2021; Received in revised form 23 October 2022; Accepted 25 October 2022
Available online 29 October 2022

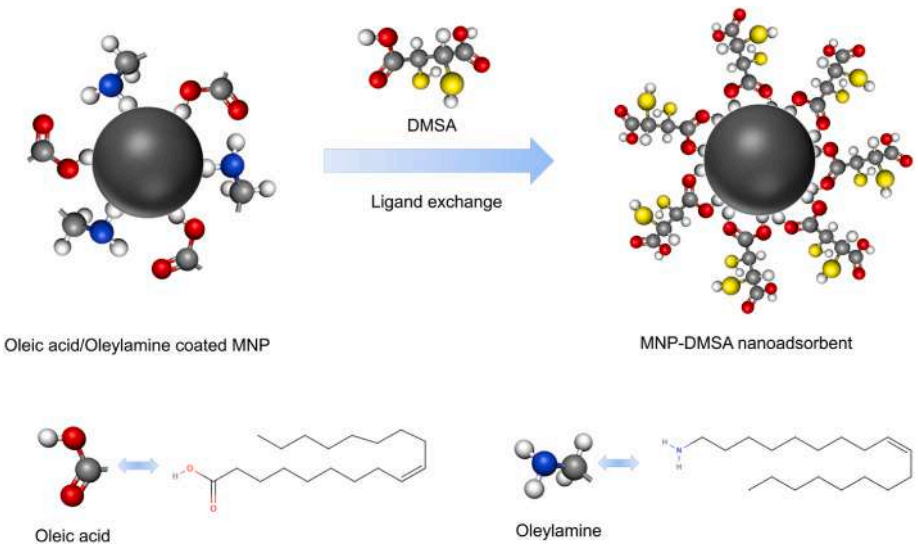

Scheme 1. Schematic representation of the ligand exchange protocol for functionalizing MNPs with DMSA. The DMSA ligands displaced the oleic acid and oleylamine surfactant moieties.

adsorption sites. For this, various linkers have been used such as ethylene diamine tetraacetic acid [16], meso-2,3-dimercaptosuccinic acid (DMSA) [15,17], chitosan [18], and (3 aminopropyl)triethoxysilane [19,20], which provide specific adsorption sites, including –COOH, $–NH_2$, –OH, and –SH [21]. MNPs functionalized with only one type of functional group are disadvantageous because they exhibit good adsorption performance with a single type of metal ion (single system) and they are less effective for the adsorption of multiple coexisting types of metal ions (e.g., ternary system) as functional groups have different binding affinities for different metal ions. The presence of different types of metal ions leads to competitive adsorption over a single functional group, thereby reducing the adsorption efficiency. In general, polluted water contains multiple HMI contaminants rather than single metal ions, thereby complicating the simultaneous removal of coexisting metal ion contaminants. Providing more than one type of functional group is expected to reduce competitive adsorption and improve the simultaneous adsorption of multiple coexisting HMIs. Thus, in the present study, Fe_3O_4 MNPs were functionalized with thiol (–SH) and carboxylic (–COOH) groups using DMSA. DMSA is a metal chelator that contains dithiol (–SH) and dicarboxylic (–COOH) groups, which chelate with HMIs by forming non-toxic complexes [22,23].

In this study, oleic acid (OA) and oleylamine (OM) coated MNPs prepared by a thermal decomposition method were functionalized with DMSA using a ligand exchange protocol. The DMSA ligands displaced the surfactant moieties due to the high coordinative capability of the first carboxyl group (see Scheme 1) [24]. The DMSA functionalized MNPs (MNP-DMSA) were used to remove coexisting Pb(II), Cd(II), and Ni(II) HMIs. Isotherm and kinetic studies were performed to describe the adsorption behavior. The simultaneous adsorption of HMIs has not been explored previously using MNP-DMSA as a nanoadsorbent.

2. Materials and methods

2.1. Chemicals

All the chemicals used in this study were analytical grade. Ferric acetylacetonate ($Fe(acac)_3$), 1,2-octanediol, and DMSA were obtained from Sigma Aldrich. Diphenyl ether (DPE), dibenzyl ether (DBE), OA, OM, dimethyl sulfoxide (DMSO), hexane, lead nitrate, cadmium sulfate, and ethanol were procured from S.D. Fine-Chem India. Nickel sulfate was supplied by Thomas Baker Pvt. Ltd. India. The pH buffer tablets and ethylenediamine-tetraacetic acid disodium salt (Na_2EDTA) were obtained from Thermo Fisher Scientific.

2.2. Synthesis of MNPs

The Fe_3O_4 MNPs were synthesized by the thermal decomposition method reported by Sun et al. [25] with slight modifications. In brief, DPE (10 mL) and DBE (10 mL) were mixed in a three-necked flask with a volume of 250 mL, where the OA (6 mmol) and OM (6 mmol) were added slowly and stirred vigorously. Under continued stirring, $Fe(acac)_3$ (2 mmol) was dissolved in the reaction mixture. Finally, 1,2-octanediol (10 mmol) was added slowly. Under an argon atmosphere, the final reaction mixture was heated to 200 °C in a heating mantle for 2 h and then refluxed at 280 °C for 1 h. The black mixture obtained was cooled down to room temperature (RT). Finally, the MNPs were centrifuged at 4000 rpm for 10 min in ethanol:hexane (1:1) to remove the reaction residuals and ligands. The resultant MNPs were dried in a vacuum desiccator.

2.3. Functionalization of MNPs with DMSA

The as-prepared MNPs were hydrophobic due to their coating with OA and OM moieties. To add the functional groups to the MNPs and make them hydrophilic, they were functionalized by DMSA using a ligand-exchange process, as reported previously [15]. First, 50 mg of MNPs were dispersed in 20 mL of toluene, before adding 5 mL of DMSO containing 90 mg of DMSA and sonicating. The solution was placed in an orbital shaker for 48 h at RT. Next, the translucent solvent containing OA and OM was discarded. The MNP-DMSA nanoadsorbents were then washed with ethanol using magnetic separation. The nanoadsorbents were then dispersed in basified Milli-Q water (pH 10) to deprotonate the carboxylic groups and thiol groups of the DMSA. The dispersed nanoadsorbents were then dialyzed in Milli-Q water for 24 h. Finally, the nanoadsorbents were redispersed in water and dried in a vacuum desiccator.

2.4. Characterization

Crystallographic characterization was conducted using a SmartLab X-ray diffractometer (Rigaku) equipped with a rotating copper anode. The diffractograms were recorded using monochromatic Cu-K_α (0.154 nm) over the angular range of 20°–100°. Transmission electron microscopy (TEM) was conducted with a model Tecnai G2 STwin, which

Table 1
Experimental conditions and parameters used in the batch adsorption experiments.

Sr. No.	Evaluated parameter	pH	Adsorbent dosage (g/L)	Contact time (min)	Initial metal ion concentration (mg/L)
1	pH	3–9	0.1	60	10
2	Adsorbent dosage (g/L)	7	0.02–0.4	60	10
3	Contact time (min)	7	0.14	10–120	10
4	Initial metal ion concentration (mg/L)	7	0.14	50	5–70

operated at a voltage of 200 kV, to determine the particle size, shape, and microstructure. Fourier transform infrared (FTIR) spectroscopy analysis was conducted for the samples using a Jasco 4600 FTIR spectrometer. The surface zeta potentials of the nanoadsorbents were measured using a Malvern Instruments Zetasizer Nano ZS90. Chemical analysis was conducted by X-ray photoelectron spectroscopy (XPS) using an ESCALAB 250Xi system (Thermo Scientific) with a monochromatic Al K_α ($h\nu = 1486.68$ eV) X-ray source for excitation. Spectral analysis and deconvolution were performed using a proprietary tool called Avantage Data System (Thermo Scientific). Magnetic measurements were performed using a Quantum Design MPMS SQUID-vibrating sample magnetometer (VSM). Magnetization loops were measured at RT (300 K) and 2 K. Thermomagnetic measurements M(T) were made between 2 K and 350 K with an applied magnetic field of 100 Oe. The specific surface area was measured according to Brunauer–Emmett–Teller (BET) theory with N_2 adsorption and desorption isotherms obtained using a Quantachrome Instruments v10.0. The concentrations of HMIs were determined with a Thermo Fisher AA203 atomic absorption spectrometer.

2.5. Batch adsorption experiments

The individual and simultaneous adsorption of Pb(II), Cd(II), and Ni(II) HMIs on MNP-DMSA nanoadsorbents were tested in aqueous solutions in batch experiments. The experiments were performed by mixing a specific amount of nanoadsorbent with a 50 mL metal ion solution in a 100 mL Erlenmeyer flask at RT. The solution was continuously shaken to reach adsorption equilibrium. The nanoadsorbents were then magnetically separated from the solution. The parameter used in the batch experiments (*i.e.*, pH, adsorbent dose, contact time, and initial concentration of HMIs) are shown in Table 1. The pH was adjusted by using pH buffer tablets. The following equations were used to calculate the removal efficiency (R) and q_e values for metal ions:

$$R\,(\%) = \frac{C_0 - C_e}{C_o} \times 100 \quad (1)$$

$$q_e = \frac{(C_0 - C_e)\,V}{m} \quad (2)$$

where:

C_0 = Initial HMI concentration (mg/L)
C_e = Equilibrium HMI concentration (mg/L)
V = Volume of HMI solution (mL) and
m = Mass of the adsorbent (mg)

In the desorption experiments, the MNP-DMSA nanoadsorbents loaded with HMIs were suspended in Na_2EDTA (25 mL, 0.1 M) for desorption. The mixture was shaken for 60 min to reach equilibrium. The MNP-DMSA was then magnetically separated. The dried MNP-DMSA was reused to adsorb the HMIs in a successive cycle.

3. Results and discussion

3.1. Characterization of MNP-DMSA nanoadsorbents

Powder X-ray diffraction (XRD) analysis was performed to study the phase and crystal structures of the MNPs. Rietveld refinement was conducted based on the XRD measurements obtained for the MNPs (Fig. 1A). The characteristic diffraction peaks for the lattice planes (220), (311), (400), (422), (511), (440), (620), (533), (444), (642), (731), and (800) in the Rietveld refined XRD patterns matched well with the magnetite phase of the cubic lattice system and Fd-3m space group (JCPDS card No. 00-019-0629). The parameters extracted after refinement of the XRD spectra are shown in Table S1. The average crystallite size calculated for the MNPs using the Debye–Scherrer equation [26] was 5.83 nm. The shapes and sizes were observed for the MNPs by TEM (Fig. 1B). The MNPs had a spherical shape and monodispersed nature. The particle size distribution (Fig. S1) obtained by evaluating multiple TEM micrographs indicated that the MNPs had an average particle size of (8.24 ± 1) nm. The inset in Fig. 1B shows the selected area electron diffraction pattern for the MNPs. The rings were indexed to the cubic structure of magnetite, which was consistent with XRD results.

The FTIR spectra obtained for MNPs and MNP-DMSA (Fig. 2A) indicated different bending and stretching vibrations. In both spectra, the strong absorption peak observed at 578 cm^{-1} was due to the Fe–O stretching vibration from MNPs [27]. In the MNPs spectrum, the peak at 1024 cm^{-1} was attributed to C–O single bond stretching from the OA chemisorbed on the surfaces of the MNPs as carboxylate [28]. The peaks at 1405 and 1602 cm^{-1} indicated NH_2 bending from OM on the surfaces of the MNPs [29]. The bands at 2850 and 2920 cm^{-1} were ascribed to symmetric and asymmetric stretching of CH_2, respectively [30]. The

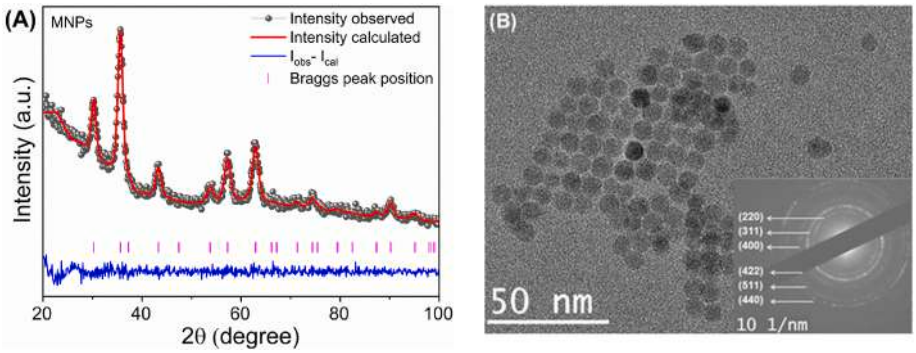

Fig. 1. (A) XRD pattern obtained for MNPs and corresponding Rietveld refinement profile using the Fullprof program. (B) TEM micrograph and electron diffraction pattern (inset) for MNPs.

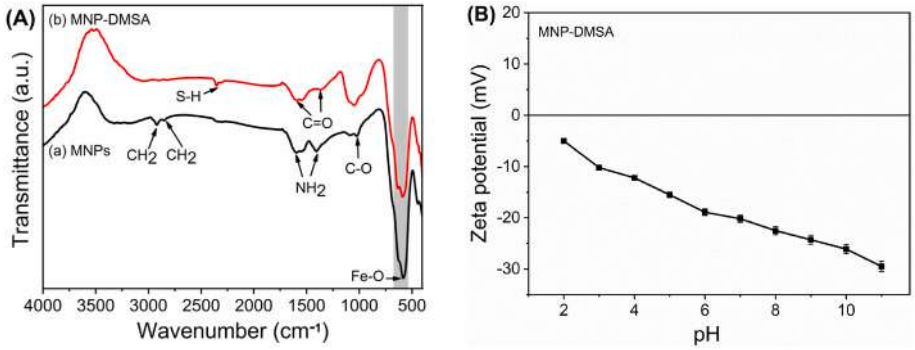

Fig. 2. (A) FTIR spectra obtained for (a) MNPs (black) and (b) MNP-DMSA (red). (B) Zeta potential measured for MNP-DMSA at different pH values.

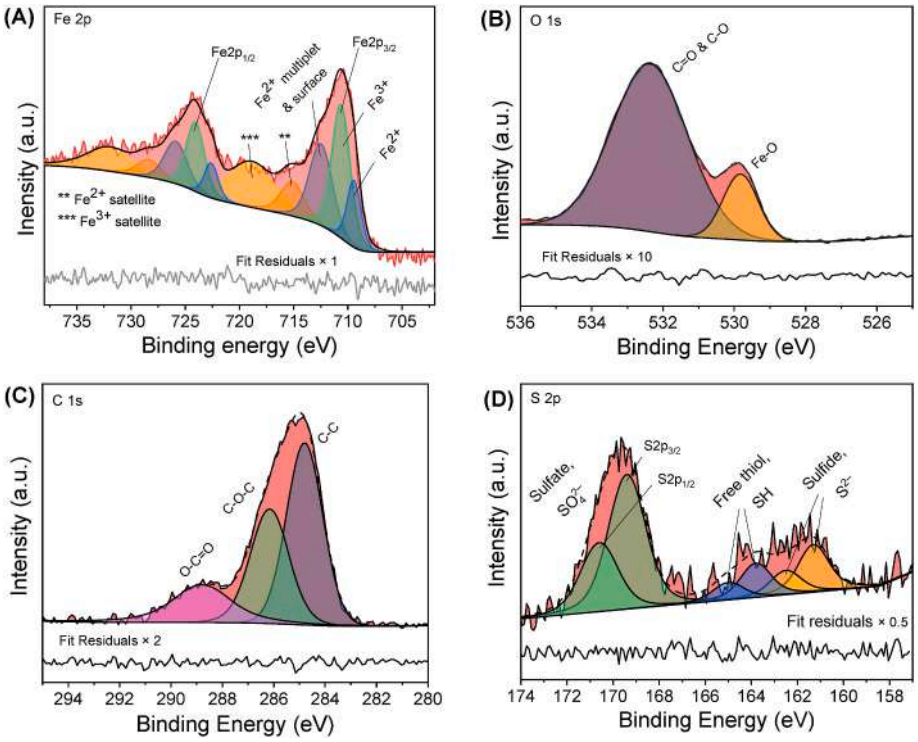

Fig. 3. High-resolution XPS spectra of Fe2p (A), O1s (B), C1s (C), and S2p (D) for MNP-DMSA.

presence of NH_2 and CH_2 groups indicated that OA and OM chemisorbed on the surfaces of the MNPs. In the MNP-DMSA spectrum, the peaks at 1594 and 1375 cm^{-1} corresponded to C═O stretching from the DMSA molecules. The peak at 2345 cm^{-1} corresponded to the thiol groups (S–H) of DMSA, which was convoluted by contamination of the CO_2 stretching bands from the background [17,31]. The presence of C═O and S–H groups indicated the successful functionalization of DMSA.

Zeta potential (ζ) measurements were performed in the pH range of 2–11 to study the surface charge and colloidal stability of the MNP-DMSA nanoadsorbents (Fig. 2B). MNP-DMSA had negative zeta potential values at all of the measured pH values, which agreed with previous studies of DMSA functionalized MNPs [32–34]. The negative surface charge of MNP-DMSA was due to ionization of the –COOH and –SH functional groups of MNP-DMSA at different pH values. The negative zeta potential indicated the hydrophilic nature of MNP-DMSA due to electrostatic repulsion. The zeta potential values around neutral pH indicated the good colloidal stability of MNP-DMSA, which is required for HMI removal applications.

XPS studies were conducted to investigate the surface composition, oxidation states, and functionalization of the MNPs. The deconvoluted XPS spectra obtained for MNP-DMSA are shown in Fig. 3. The Fe 2p spectrum contained broad features (Fig. 3A) that could not be adequately attributed to only one Fe^{2+} or Fe^{3+} spin-orbit and crystal field multiplets, thereby indicating a mixture of iron valence states [35–37]. The Fe 2p spectrum was fitted according to the simplified scheme used previously to deconvolve the Fe 2p spectra of Fe_3O_4 [36]. The Fe $2p_{3/2}$ component of the high-spin Fe^{3+} multiplet was approximated by one peak and the high-spin Fe^{2+} multiplet was approximated by two features separated by ~3 eV. Given the small size and developed surfaces of the MNPs, we could not exclude assigning the last peak to surface states [37]. The Fe^{2+} and Fe^{3+} shake-up satellite peaks were positioned ~6 and ~8 eV higher than the corresponding main Fe $2p_{3/2}$ peaks. After fitting with the given number of peaks and considering the spin-orbit splitting of 13.2 ± 0.1 eV and full width at half-maximum of the main peaks <2.0 eV, the high-resolution Fe 2p core-level spectrum indicated binding energies for the Fe^{2+} and Fe^{3+} $2p_{3/2}$ peaks of 709.4 and 710.6 eV, respectively, and for their respective satellite peaks of 715.1 eV and 718.9 eV (Fig. 3A and Table S2). The position of the Fe 2p peak was consistent with previously reported values [37]. The shift in the binding energy values could have been due to charge correction and

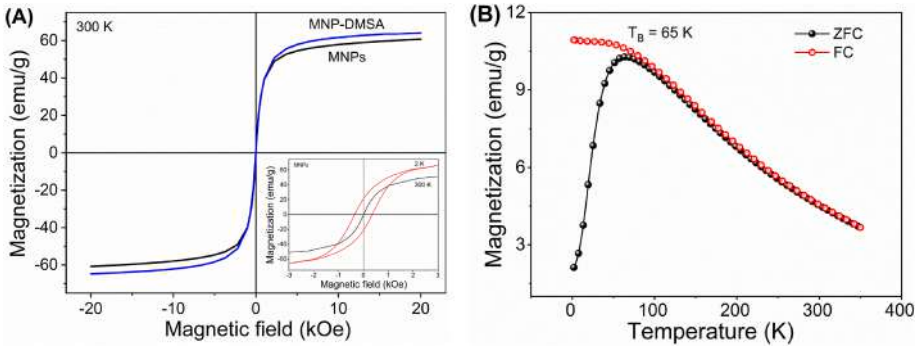

Fig. 4. (A) Magnetization curves measured for MNPs and MNP-DMSA at 300 K, where the inset shows the low field magnetization curves for MNPs, which indicate the increase in the coercive field at 2 K compared with 300 K. (B) Zero field cooled (ZFC) and field cooled (FC) curves for MNPs, with a clear phase transition.

slight errors in the multicomponent fitting process. The resulting Fe^{3+}/Fe^{2+} ratio of 72:28 is quite close to the ideal ratio in magnetite of 67:33, thereby supporting the reliability of the fit and demonstrating the presence of the Fe_3O_4 structural configuration [38]. In the O 1s spectrum, the peak at 529.8 eV was associated with Fe bound oxygen and the peak at 532.3 eV was consistent with the binding energies reported previously for organic C═O [39,40]. In addition to the adventitious carbon at 284.8 eV (used as a charge reference), the binding energies of 288.8 and 286.2 eV for the C 1s state indicated the presence of O–C═O and C–O–C in DMSA, respectively [41,42]. The S 2p spectrum was optimally fitted with three spin-orbit doublets (splitting of 1.2 ± 0.1 eV and full width at half-maximum <1.9 eV) with S $2p_{3/2}$ peaks at 161.3, 163.8 eV, and 169.4 eV (Fig. 3D and Table S3). The first peak at 161.3 eV was assigned to metal sulfide [43], which may have indicated partial sulfidation of iron near the surface, *i.e.*, Fe oxide/Fe sulfide core–shell formation. The second component could be assigned to a free thiol group typically at ~163.5 eV [44]. This type of sulfur was due to DMSA ligands and this finding agreed with the FTIR results, where S–H bonds were detected due to characteristic vibrations (Fig. 2A). The shift of the third doublet to a significantly higher binding energy indicated oxidized sulfur, e.g., SO_4^{2-} or SO_4H^- [45], which may have formed due to the storage and processing of the samples in air.

The magnetization hysteresis loops recorded for MNPs and MNP-DMSA by SQUID-VSM at RT are presented in Fig. 4A. The magnetic measurements suggested that the MNPs and MNP-DMSA exhibited a superparamagnetic response with negligible coercive and remanence fields at RT, whereas the coercivity of the as-prepared MNPs reached 355 Oe when measured at 2 K (see the inset in Fig. 4A). The saturation magnetization values were calculated for both MNPs and MNP-DMSA by linear extrapolation of the magnetization, M, in the high field region from M vs 1/H when 1/H → 0. The saturation magnetization (M_s) value recorded for MNPs at RT was 62.8 emu/g, which was less than the value for bulk magnetite of 94 emu/g [46]. This decrease in M_s may have been due to spin disorder or a magnetic dead layer on the surface of the MNPs [47]. After functionalizing the MNPs with DMSA, the M_S value at RT increased slightly to 66 emu/g. A similar increase in M_S after DMSA functionalization was reported in previous studies [48,49]. The increase in M_S for MNP-DMSA was due to the replacement of high molecular weight OA/OM molecules by lower molecular weight DMSA during the ligand exchange process. In addition, during the cleaning process, the small MNPs that did not settle rapidly on the magnet were discarded. These discarded nanoparticles were less magnetic due to their smaller size, and thus their removal resulted in higher normalized magnetization. Fig. 4B shows the magnetization versus temperature curves for the MNPs under zero field cooling and field cooling conditions. The phase transformation temperature at which the MNPs underwent a transition from the superparamagnetic state to the ferromagnetic state (and vice versa), also known as blocking temperature (T_B), was 65 K. According to T_B and previously reported values of the anisotropy constant K (1.35×10^4 J/m^3) [50], the average size of the MNPs was calculated using the equation: $T_B = VK/25k_B$, where V is the volume of the MNP and k_B is the Boltzmann constant. The average particle size was estimated as ~7.2 ± 1 nm considering spherical geometry. The apparent difference in the estimated size of the MNPs can be explained by TEM measuring the physical size, which included the dead magnetic or spin disordered layer surrounding the MNPs, whereas the size calculated based on T_B only considered the magnetically active core. Thus, the difference in these measurement methods provided a fair estimate of a magnetic dead mantle with a thickness of ~1 nm around the MNPs.

The surface areas of the bare and functionalized MNPs were analyzed using nitrogen adsorption–desorption isotherms based on BET theory (Fig. S2). The BET surface areas of the bare MNPs and MNP-DMSA were calculated as 123 and 137 m^2/g, respectively. The increase in the surface area of MNP-DMSA was due to the effect of functionalization with DMSA

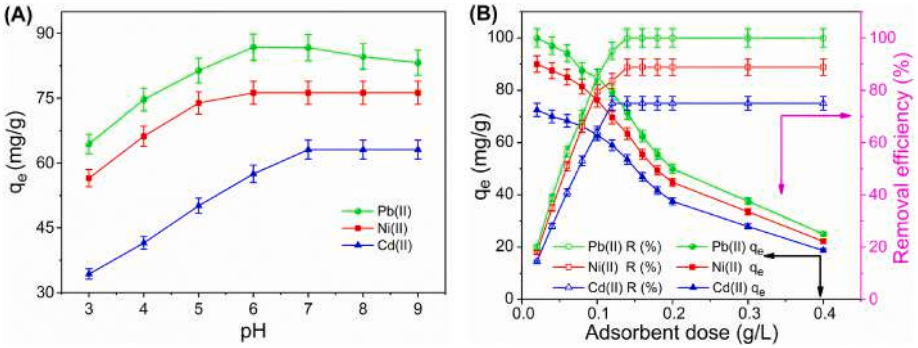

Fig. 5. (A) Effects of pH on the adsorption capacity (q_e) of Pb(II), Cd(II), and Ni(II) by MNP-DMSA nanoadsorbents (initial metal ion concentration = 10 mg/L, adsorbent dose = 0.1 g/L, and contact time = 60 min). (B) Effects of adsorbent dose on the adsorption capacity (q_e) and removal efficiency (R) of Pb(II), Cd(II), and Ni(II) by the MNP-DMSA nanoadsorbents (pH = 7, initial metal ion concentration = 10 mg/L, and contact time = 60 min).

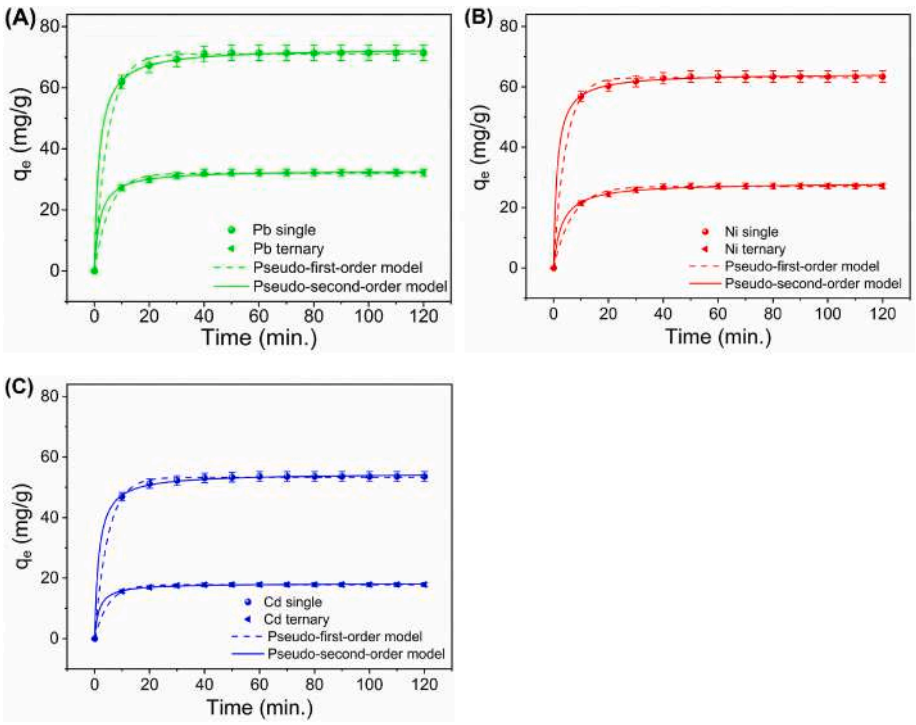

Fig. 6. Effects of the contact time on the adsorption capacities (q_e) of MNP-DMSA nanoadsorbents, and adsorption kinetics in the single and ternary systems for (A) Pb(II), (B) Ni(II), and (C) Cd(II) (initial metal ion concentration = 10 mg/L, adsorbent dose = 0.14 g/L, and pH = 7).

on the MNPs. The increase in the BET surface area could have helped to improve the q_e for the HMI removal process [51].

3.2. Adsorption studies

3.2.1. Effects of initial pH and adsorbent dose

The pH of a solution is a fundamental parameter that influences the q_e values of adsorbents because it affects the available active sites on the nanoadsorbent [52,53]. Initially, the pH of the aqueous solution was 7.3. The effects of pH on the q_e values for Pb(II), Cd(II), and Ni(II) on the MNP-DMSA nanoadsorbent were studied in the pH range from 3 to 9 (Fig. 5A). For Pb(II) and Ni(II), as the pH increased, q_e increased and the maximum value was obtained at pH 6. The q_e value for Ni(II) saturated above pH 6. The aqueous Pb(II) solution was slightly turbid above pH 7 and the q_e value decreased slightly. For Cd(II), the maximum q_e value occurred at pH 7 and it saturated at higher pH values. Speciation diagrams for Pb(II), Ni(II), and Cd(II) metal ions were plotted using visual MINTEQ 3.1 (Fig. S3). At pH < 6, Pb(II) species were dominant. Hence, the adsorption capacity increased as the pH increased up to 7. As the pH increased above 6, the formation of complex ions or precipitates of Pb (II) occurred $(Pb(OH)^{+}$, $(Pb_3OH_4)^{2+}$, etc.), which affected the interaction between the active adsorption sites and Pb(II) metal ions [5]. For Ni (II) and Cd(II) metal ions, no hydroxyl species or complexes formed up to pH 8. However, above pH 8, various metal complexes formed in the Ni (II) and Cd(II) solutions. Divalent cations were dominant for Pb(II), Ni (II), and Cd(II) in the pH range of 6–7. Therefore, pH 7 was selected for further adsorption experiments because q_e was maximized at this pH value.

The q_e and R values as functions of the adsorbent dose are shown in Fig. 5B. The adsorbent dose was varied from 0.02 g/L to 0.4 g/L with a constant initial HMI concentration (10 mg/L) and pH (7). Up to an adsorbent dose of 0.1 g/L, a linear increase in R was observed for the HMIs due to the availability of vacant adsorption sites. However, further increasing the adsorbent dose resulted in a saturation region and no significant increase in R occurred subsequently. The R value for Cd(II) reached equilibrium at a dose of 0.12 g/L. By contrast, the adsorbent dose required for Pb(II) and Ni(II) to reach equilibrium was 0.14 g/L. As the adsorbent dose increased, the q_e values decreased for all three metals ions. At higher adsorbent doses, the active adsorption sites were not completely occupied because of the decreased interaction between HMIs and the adsorbent due to the lack of HMIs relative to the available binding sites [5,54]. In addition, at a high adsorbent dose, the aggregation of adsorbents may have reduced the surface area [55]. In subsequent experiments, an adsorbent dose of 0.14 g/L was used as the optimum dose.

Table 2
Parameters of the kinetic models for the adsorption of Pb(II), Cd(II), and Ni(II) metal ions on MNP-DMSA nanoadsorbents in single and ternary systems.

Metal ion	q_e(exp.) (mg/g)	Pseudo-first order (PFO)				Pseudo-second order (PSO)			
		q_e(cal.) (mg/g)	k_1 (/min)	R^2	χ^2	q_e(cal.) (mg/g)	k_2 (g/mg/min)	R^2	χ^2
Pb(II) single	71.42	71.02	0.198	0.9976	0.8966	71.72	0.0079	0.9993	0.2653
Ni(II) single	63.42	63.05	0.2244	0.9981	0.62744	63.70	0.0117	0.9997	0.09023
Cd(II) single	53.57	53.29	0.2066	0.9987	0.2808	53.84	0.01186	0.9995	0.1143
Pb(II) ternary	32.14	31.99	0.18	0.9975	0.1911	32.25	0.0151	0.9987	0.10039
Ni(II) ternary	27.14	26.97	0.1477	0.9961	0.23371	27.40	0.01185	0.9981	0.11233
Cd(II) ternary	17.85	17.65	0.20497	0.9984	0.0382	18.08	0.03508	0.9993	0.01745

Note: q_e(exp.) and q_e(cal.) are the equilibrium experimental and calculated adsorption capacities at time t, respectively. R^2 is the correlation coefficient and χ^2 is the Chi-square value.

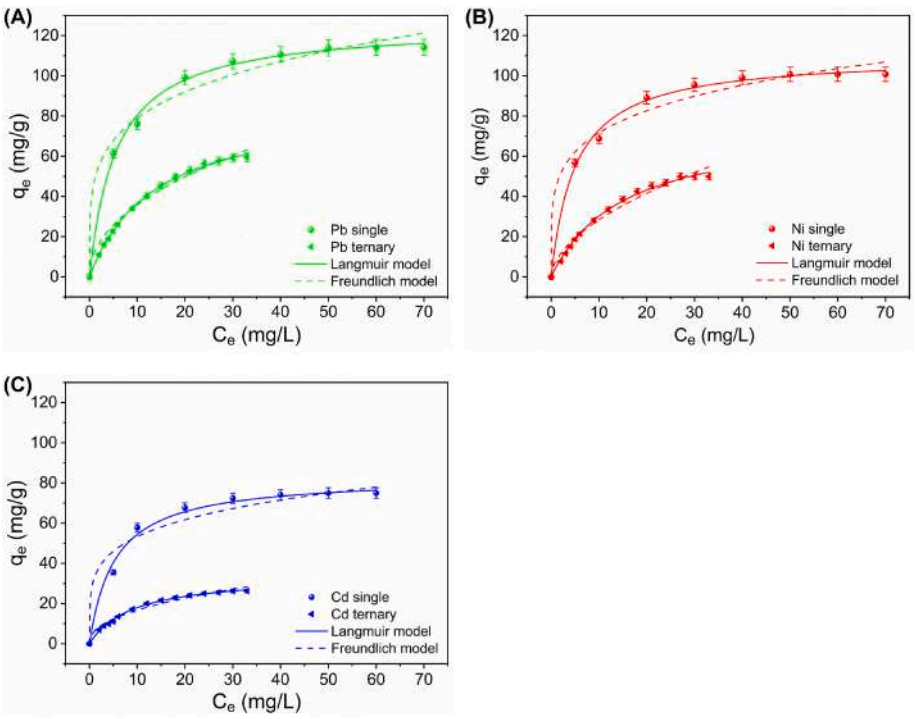

Fig. 7. Effects of the initial concentrations of heavy metal ions on the adsorption capacity of MNP-DMSA nanoadsorbents, and adsorption isotherms for (A) Pb(II), (B) Ni(II), and (C) Cd(II) in single and ternary systems (pH = 7, adsorbent dose = 0.14 g/L, and contact time = 50 min).

3.2.2. Adsorption kinetics of single and ternary metal ion systems

The adsorption process depends on the physical and chemical properties of the adsorbent. The dependences of q_e on the contact time for Pb(II), Cd(II), and Ni(II) HMIs are shown in Fig. 6. Initially, q_e increased rapidly with the contact time because many adsorbent sites were vacant [15]. After about 50 min, the adsorption curves reached equilibrium for Pb(II) and Ni(II). In the case of Cd(II), the adsorption equilibrium was reached after 40 min. The q_e value was lower for the ternary metal ion system than the single systems due to the strong competition between multiple coexisting HMIs hindering the interactions between HMIs and the binding sites on MNP-DMSA. The adsorption behaviors of HMIs on MNP-DMSA nanoadsorbents were studied by using pseudo-first order (PFO) and pseudo-second order (PSO) kinetic models. The nonlinear forms of the PFO [56] and PSO kinetic models, respectively, are expressed as follows [57]:

$$q_t = q_e - q_e e^{-k_1 t} \tag{3}$$

$$q_t = \frac{k_2 q_e^2 t}{1 + k_2 q_e t} \tag{4}$$

where q_e (mg/g) and q_t (mg/g) are the adsorption capacities at equilibrium and time t (min), respectively, and k_1 (/min) and k_2 (g/mg/min) are the rate constants for PFO and PSO kinetic models, respectively. The experimental data fitted with the PFO and PSO models are shown in Fig. 6A–C. The corresponding values of the kinetic parameters are presented in Table 2. The correlation coefficients (R^2) value were similar for both the PFO and PSO kinetic models, so it was difficult to determine the best kinetic model for describing the metal ion adsorption process based on the R^2 values. Hence, the chi-square test was used to confirm the kinetic model with the best fit [53,58]. The chi-square value is calculated as follows.

$$\chi^2 = \sum_{i=1}^{n} \frac{(q_e - q_m)^2}{q_m}$$

However, the χ^2 values obtained for both the models did not differ greatly considering the error bars. Hence, based on the χ^2 values alone, we could not differentiate between the PFO and PSO models. The high-resolution XPS spectra obtained for the spent nanoadsorbent are discussed in the following. The XPS results obtained for the spent nanoadsorbents showed that metal ions adsorbed on the surfaces of the MNP-DMSA nanoadsorbents through complexation reactions (chemisorption). Thus, the XPS results supported the PSO model. Further investigations were conducted to understand the actual kinetic process.

3.2.3. Adsorption isotherms for single and ternary metal ion systems

Adsorption isotherm models were used to study the adsorption behavior of HMIs, the competitive effect between HMIs, and the surface properties of the nanoadsorbents [5,59]. The adsorption isotherms (Fig. 7) showed that q_e increased as the HMI concentrations increased, and equilibrium was reached above a specific initial HMI concentration. Equilibrium was reached when the active adsorption sites were entirely occupied by metal ions [52]. To study the adsorption mechanism, Langmuir and Freundlich isotherm models were applied to the experimental data obtained for the single and ternary metal ion systems. The nonlinear form of the Langmuir isotherm model is expressed as [60]:

$$q_e = \frac{K_L q_m C_e}{1 + K_L C_e} \tag{5}$$

where K_L is the Langmuir adsorption constant (L/mg) and q_m is the maximum adsorption capacity (mg/g). The Langmuir isotherm model is based on the assumption of homogeneous monolayer chemisorption between adsorbates and adsorbents with a limited number of adsorption sites [54,61]. The Langmuir isotherm model predicts the favorability or unfavorability of adsorption in terms of a separation factor (R_L) calculated as follows [62].

$$R_L = \frac{1}{1 + K_L C_0} \tag{6}$$

The nonlinear form of the Freundlich isotherm model is expressed as [63]:

Table 3
Parameters of the isotherm models for the adsorption of Pb(II), Cd(II), and Ni(II) metal ions on MNP-DMSA nanoadsorbents in single and ternary metal ion systems.

Metal ion	q_e(exp.) (mg/g)	Langmuir model			Freundlich model		
		q_m(cal.) (mg/g)	K_L (L/mg)	R^2	K_F (L/mg)	n	R^2
Pb(II) single	114.18	116.54	0.172	0.9996	50.34	4.34	0.9050
Ni(II) single	100.79	102.73	0.19	0.9994	43.65	4.27	0.9074
Cd(II) single	74.92	75.48	0.56	0.9993	49.068	8.5	0.9896
Pb(II) ternary	60.14	64.5	0.07318	0.9984	17.19	2.92	0.9176
Ni(II) ternary	50.20	53.9	0.07331	0.9959	10.14	2.1	0.9659
Cd(II) ternary	26.43	27.18	0.1109	0.9962	6.072	2.27	0.9771

Note: q_e(exp.) and q_m(cal.) are the experimental and maximum adsorption capacities, respectively. R^2 is the correlation coefficient.

Table 4
Adsorption capacity of the MNP-DMSA nanoadsorbent compared with those of previously reported magnetic adsorbents for the removal of Pb (II), Ni(II), and Cd(II) in single metal ion systems.

Adsorbent	Adsorption capacity for heavy metal ions (mg/g)			Reference
	Pb(II)	Ni(II)	Cd (II)	
Carboxymethyl-cyclodextrin polymer grafted on Fe_3O_4	64.5	13.2	27.7	[71]
NH_2 functionalized magnetic graphene composite	27.95	22.07	27.83	[72]
NH_2-MCM-41 nanoparticle	57.74	12.36	18.25	[73]
OP/Fe_3O_4 magnetic composite	54.94	51.81	–	[74]
Cysteine-functionalized Fe_3O_4@SiO_2 nanoparticles	81.8	–	–	[75]
Amino-functionalized Fe_3O_4 magnetic nanoparticles	40.1	–	–	[76]
Asparagine functionalized Fe_3O_4	–	87.18	–	[77]
Sodium dodecyl sulfate-coated magnetite nanoparticles	–	41.2	–	[78]
3-Mercaptopropionic acid functionalized Fe_3O_4 nanoparticles	–	42.01	–	[79]
Carboxyl-modified Fe_3O_4@SiO_2 nanoparticles	–	63.99	–	[80]
Shellac-coated iron oxide	–	–	18.8	[81]
Magnetic chitosan nanoparticles	–	–	36.42	[82]
MNP-DMSA	116.54	102.73	75.48	**Present study**

$$q_e = K_F C_e^{\frac{1}{n}} \quad (7)$$

where K_F and n are Freundlich constants related to the adsorption capacity (L/g) and heterogeneity factor (mg/g), respectively. The Freundlich isotherm model assumes multilayer and heterogeneous physisorption, where the number of adsorption sites varies [54].

The experimental data obtained for the single and ternary metal ion systems were fitted to approximate simple Langmuir and Freundlich models (Fig. 7A–C). The fitting parameters obtained for the simple Langmuir model were averaged for all thiol and carboxylic sites, and the total adsorption capacity was the sum for the two types of sites. The values obtained for the parameters are presented in Table 3, which shows that for the single and ternary systems, the R^2 values for the Langmuir model were $0.9993 < R^2 < 0.9996$ and $0.9996 < R^2 < 0.9998$, respectively. However, the R^2 values for the Freundlich model were $0.9050 < R^2 < 0.9896$ and $0.8681 < R^2 < 0.9918$ for the single and ternary HMI systems, respectively. Thus, for both the single and ternary HMI systems, the R^2 values were higher for the Langmuir model than the Freundlich model. Moreover, the q_e values calculated using the Langmuir model agreed well with the experimental q_e values for both the single and ternary HMI systems. Hence, the Langmuir model was considered a better fit to the observed data, thereby indicating that homogeneous monolayer adsorption of HMIs occurred on the MNP-DMSA nanoadsorbents in both the single and ternary HMIs systems. The R_L values calculated with Eq. (6) ranged between 0 and 1, thereby indicating that adsorption was favorable [62].

According to the simple Langmuir model, the q_m values obtained for Pb (II), Ni(II), and Cd(II) in the single systems were 116.54, 102.73, and 75.48 mg/g, respectively. The q_m values for Pb (II), Ni(II), and Cd(II) are compared with previously reported values for other adsorbents in Table 4. During the simultaneous removal of HMIs from the ternary metal ion system, the q_m values for Pb (II), Ni(II), and Cd(II) decreased to 64.5, 53.9, and 27.18 mg/g, respectively. The decreases in the q_m values in the ternary system were due to the competition between different HMIs for occupying binding sites [51]. A higher K_L value indicates greater affinity between the adsorbent and metal ions. In the present study, K_L value was greater for Cd(II) than the other metals in the single and ternary systems. Thus, Cd(II) had a greater affinity for the MNP-DMSA nanoadsorbent than Pb(II) and Ni(II) [5].

The XPS survey spectra obtained for MNP-DMSA before and after the adsorption of HMIs are shown in Supplementary Material Fig. S4A. After the adsorption of metal ions, new peaks corresponding to Pb(II), Ni(II), and Cd(II) were observed at binding energies of 139.7 eV, 847 eV, and 412 eV, respectively. However, in the survey spectrum for MNP-DMSA-Ni(II), at a binding energy of 847 eV, the Fe2p peak overlapped greatly with the Ni(II) peak. Thus, the XPS survey spectra obtained for the spent sorbent indicated the adsorption of Pb(II), Ni(II), and Cd(II) on the surfaces of the MNP-DMSA nanoadsorbents. The high-resolution spectra for the absorbed Pb(II) metal ions indicated the formation of a bidentate complex on the surface of MNP-DMSA, and the two peaks for $Pb4f_{7/2}$ and $Pb4f_{5/2}$ (Fig. S4B) had binding energies of 138.9 eV and 143.7 eV, respectively [64]. The XPS spectra obtained for Ni(II) loaded on the nanoadsorbent contained two peaks for Ni $2p_{3/2}$ and Ni $2p_{1/2}$. The Ni $2p_{3/2}$ peak was deconvoluted into two peaks with binding energies of 856.4 eV (Ni $2p_{3/2}$) and 862.2 eV (Ni $2p_{3/2}$ satellite) (Fig. S4C). In addition, the Ni $2p_{1/2}$ peak was deconvoluted into two peaks with binding energies of 875 eV (Ni $2p_{1/2}$) and 879.4 eV (Ni $2p_{1/2}$ satellite) [65]. The high-resolution spectra obtained for Cd(II) contained two peaks at binding energies of 405.6 eV and 412.3 eV, which were attributed to $Cd3d_{5/2}$ and $Cd3d_{3/2}$ (Fig. S4D), respectively, and they indicated the binding of Cd(II) on the surface of the nanoadsorbent [66]. Thus, the high-resolution XPS spectra obtained for the nanoadsorbents loaded with heavy metals showed that metal ions adsorbed on the surfaces of the MNP-DMSA nanoadsorbents through complexation reactions (chemisorption).

The order of the q_e values for MNP-DMSA in both the single and ternary systems was: Pb(II) > Ni(II) > Cd(II). The observed variations in the capacities to adsorb different HMIs were clarified by considering the hydration radius and electronegativity in the adsorption process. The hydration radius of Pb(II) (4.01 nm) is smaller compared with those of Ni(II) (4.04 nm) and Cd(II) (4.26 nm), so Pb(II) tended to have higher q_e values because these ions diffused swiftly on the surface and pores of the adsorbent due to the lower diffusion resistance [67,68]. In addition, the electronegativity of Pb(II) (2.33) is higher compared with those of the other two metal ions comprising Ni(II) (1.91) and Cd(II) (1.69), and thus Pb(II) ions were strongly attracted toward the nanoadsorbent to form complexes with the functional groups [69,70].

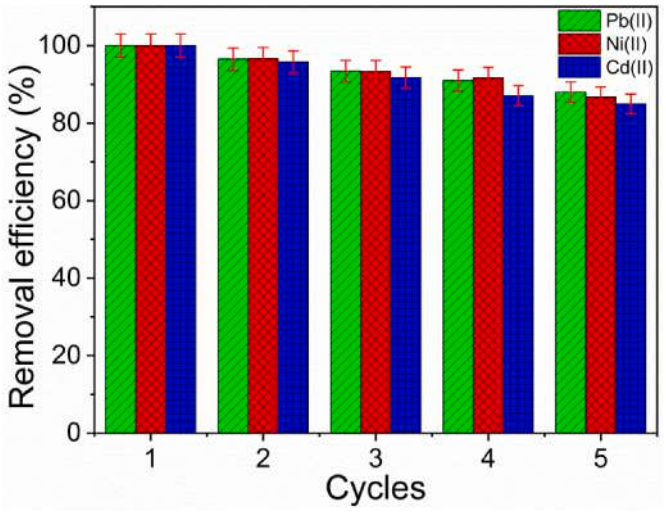

Fig. 8. Reusability of MNP-DMSA nanoadsorbent for the adsorption/desorption of Pb(II), Ni(II), and Cd(II).

3.3. Desorption and reusability study

The reusability of the MNP-DMSA nanoadsorbent was evaluated over five successive cycles in adsorption–desorption experiments. The reusability results are shown in Fig. 8. After five consecutive adsorption/desorption cycles, the Pb(II), Ni(II), and Cd(II) removal efficiencies decreased by 12%, 13%, and 15%, respectively. Clearly, MNP-DMSA exhibited good regeneration performance, and thus it may be reused as an efficient nanoadsorbent.

4. Conclusions

In this study, monodispersed Fe_3O_4 MNPs were successfully functionalized by DMSA using the ligand exchange process. The resulting colloidal, stable MNP-DMSA was used as an effective nanoadsorbent to simultaneously remove Pb(II), Cd(II), and Ni(II) metal ions from aqueous solutions. The MNPs had a pure magnetite phase and spherical shape with an average particle size of 8.24 ± 1 nm. FTIR and XPS analyses demonstrated the presence of carboxyl and thiol-functional groups on MNP-DMSA. The MNPs were superparamagnetic at RT with a M_s value of 62.8 emu/g. Analysis based on BET theory determined surface areas of 123 and 137 m^2/g for MNPs and MNP-DMSA, respectively. Zeta potential measurements indicated the hydrophilic nature and good colloidal stability of MNP-DMSA due to the increased negative surface charge compared with the bare MNPs.

The experimental data followed the Langmuir model, thereby suggesting homogeneous monolayer adsorption of HMIs on the surfaces of the nanoadsorbents in both the single and ternary HMIs systems. Kinetic studies showed that both the single and ternary metal ion systems followed the PSO kinetic model, and thus the chemisorption process was mediated by the active carboxylic and thiol groups of the MNP-DMSA nanoadsorbent. The q_e values obtained for Pb(II), Ni(II), and Cd(II) in the present study were higher than those reported in previous studies [71–73]. The lower hydration radius and higher electronegativity of Pb(II) was responsible for its greater adsorption compared with the other metals. The MNP-DMSA nanoadsorbent exhibited good reusability performance in five adsorption/desorption cycles. The results obtained in this study demonstrate that the MNP-DMSA nanoadsorbent is a promising material for the simultaneous removal of multiple HMIs from aqueous solution.

Credit author statement

P.B. Patil: Conceptualization, methodology and experimental supervision, draft revision.

V.P. Kothavale, A. Sharma, V.D. Chavan, and S.R. Shingte: Data curation, writing-original draft.

A. Sharma, R.P. Dhavale, O. Selyshchev, and T.D. Dongale: Materials characterization.

D.R.T. Zahn, G. Salvan, and H.H. Park: Review and editing.

Declaration of competing interest

The authors declare that they have no known competing financial interests or personal relationships that could have appeared to influence the work reported in this paper.

Data availability statement

Data will be made available on request.

Acknowledgments

P.B. Patil would like to acknowledge the Science and Engineering Research Board, Department of Science and Technology (DST-SERB), Government of India for financial support (No. EMR/2017/001810). A. Sharma and G. Salvan acknowledge the financial support provided by the Deutsche Forschungsgemeinschaft (DFG) under project number 282193534. R.P. Dhavale and H.H. Park would like to acknowledge that this study was supported by a National Research Foundation of Korea (NRF) grant funded by the Korean government (MSIT) (No. 2020R1A5A1019131).

Appendix A. Supplementary data

Supplementary data to this article can be found online at https://doi.org/10.1016/j.jpcs.2022.111089.

References

[1] M.R. Lasheen, I.Y. El-Sherif, M.E. Tawfik, S.T. El-Wakeel, M.F. El-Shahat, Preparation and adsorption properties of nano magnetite chitosan films for heavy metal ions from aqueous solution, Mater. Res. Bull. 80 (2016) 344–350, https://doi.org/10.1016/j.materresbull.2016.04.011.

[2] M.J.K. Ahmed, M. Ahmaruzzaman, A review on potential usage of industrial waste materials for binding heavy metal ions from aqueous solutions, J. Water Proc. Eng. 10 (2016) 39–47, https://doi.org/10.1016/j.jwpe.2016.01.014.

[3] Y.M. Hao, C. Man, Z.B. Hu, Effective removal of Cu (II) ions from aqueous solution by amino-functionalized magnetic nanoparticles, J. Hazard Mater. 184 (2010) 392–399, https://doi.org/10.1016/j.jhazmat.2010.08.048.

[4] J.F. Liu, Z.S. Zhao, G. Bin Jiang, Coating Fe_3O_4 magnetic nanoparticles with humic acid for high efficient removal of heavy metals in water, Environ. Sci. Technol. 42 (2008) 6949–6954, https://doi.org/10.1021/es800924c.

[5] H. Wang, Z. Wang, R. Yue, F. Gao, R. Ren, J. Wei, X. Wang, Z. Kong, Functional group-rich hyperbranched magnetic material for simultaneous efficient removal of heavy metal ions from aqueous solution, J. Hazard Mater. 384 (2020), 121288, https://doi.org/10.1016/j.jhazmat.2019.121288.

[6] F. Ge, M.-M. Li, H. Ye, B.-X. Zhao, Effective removal of heavy metal ions Cd^{2+}, Zn^{2+}, Pb^{2+}, Cu^{2+} from aqueous solution by polymer-modified magnetic nanoparticles, J. Hazard Mater. 211–212 (2012) 366–372, https://doi.org/10.1016/j.jhazmat.2011.12.013.

[7] N.C. Feitoza, T.D. Gonçalves, J.J. Mesquita, J.S. Menegucci, M.K.M.S. Santos, J. A. Chaker, R.B. Cunha, A.M.M. Medeiros, J.C. Rubim, M.H. Sousa, Fabrication of glycine-functionalized maghemite nanoparticles for magnetic removal of copper from wastewater, J. Hazard Mater. 264 (2014) 153–160, https://doi.org/10.1016/j.jhazmat.2013.11.022.

[8] M. Ozmen, K. Can, G. Arslan, A. Tor, Y. Cengeloglu, M. Ersoz, Adsorption of Cu(II) from aqueous solution by using modified Fe_3O_4 magnetic nanoparticles, Desalination 254 (2010) 162–169, https://doi.org/10.1016/j.desal.2009.11.043.

[9] U.C. Ugochukwu, M.D. Jones, I.M. Head, D.A.C. Manning, C.I. Fialips, Biodegradation and adsorption of crude oil hydrocarbons supported on "homoionic" montmorillonite clay minerals, Appl. Clay Sci. 87 (2014) 81–86, https://doi.org/10.1016/j.clay.2013.11.022.

[10] F. Di Natale, A. Erto, A. Lancia, Desorption of arsenic from exhaust activated carbons used for water purification, J. Hazard Mater. 260 (2013) 451–458, https://doi.org/10.1016/j.jhazmat.2013.05.055.

[11] K. Rida, S. Bouraoui, S. Hadnine, Adsorption of methylene blue from aqueous solution by kaolin and zeolite, Appl. Clay Sci. 83–84 (2013) 99–105, https://doi.org/10.1016/j.clay.2013.08.015.

[12] F. Cao, P. Yin, X. Liu, C. Liu, R. Qu, Mercury adsorption from fuel ethanol onto phosphonated silica gel prepared by heterogenous method, Renew. Energy 71 (2014) 61–68, https://doi.org/10.1016/j.renene.2014.05.028.

[13] S.C.N. Tang, I.M.C. Lo, Magnetic nanoparticles: essential factors for sustainable environmental applications, Water Res. 47 (2013) 2613–2632, https://doi.org/10.1016/j.watres.2013.02.039.

[14] S.H. Huang, D.H. Chen, Rapid removal of heavy metal cations and anions from aqueous solutions by an amino-functionalized magnetic nano-adsorbent, J. Hazard Mater. 163 (2009) 174–179, https://doi.org/10.1016/j.jhazmat.2008.06.075.

[15] V.D. Chavan, V.P. Kothavale, S.C. Sahoo, P. Kollu, T.D. Dongale, P.S. Patil, P. B. Patil, Adsorption and kinetic behavior of Cu(II) ions from aqueous solution on DMSA functionalized magnetic nanoparticles, Phys. B Condens. Matter 571 (2019) 273–279, https://doi.org/10.1016/j.physb.2019.07.026.

[16] E. Ghasemi, A. Heydari, M. Sillanpää, Superparamagnetic Fe_3O_4@EDTA nanoparticles as an efficient adsorbent for simultaneous removal of Ag(I), Hg(II), Mn(II), Zn(II), Pb(II) and Cd(II) from water and soil environmental samples, Microchem. J. 131 (2017) 51–56, https://doi.org/10.1016/j.microc.2016.11.011.

[17] W. Yantasee, C.L. Warner, T. Sangvanich, R.S. Addleman, T.G. Carter, R.J. Wiacek, G.E. Fryxell, C. Timchalk, M.G. Warner, Removal of heavy metals from aqueous systems with thiol functionalized superparamagnetic nanoparticles, Environ. Sci. Technol. 41 (2007) 5114–5119, https://doi.org/10.1021/es0705238.

[18] P.P. Waifalkar, S.B. Parit, A.D. Chougale, S.C. Sahoo, P.S. Patil, P.B. Patil, Immobilization of invertase on chitosan coated γ-Fe_2O_3 magnetic nanoparticles to facilitate magnetic separation, J. Colloid Interface Sci. 482 (2016) 159–164, https://doi.org/10.1016/j.jcis.2016.07.082.

[19] P.B. Patil, V.C. Karade, P.P. Waifalkar, S.C. Sahoo, P. Kollu, M.S. Nimbalkar, A. D. Chougale, P.S. Patil, Functionalization of magnetic hollow spheres with (3-aminopropyl)triethoxysilane for controlled drug release, IEEE Trans. Magn. 53 (2017), https://doi.org/10.1109/TMAG.2017.2706949, 1–1.

[20] R.P. Dhavale, P.P. Waifalkar, A. Sharma, R.P. Dhavale, S.C. Sahoo, P. Kollu, A. D. Chougale, D.R.T. Zahn, G. Salvan, P.S. Patil, P.B. Patil, Monolayer grafting of aminosilane on magnetic nanoparticles: an efficient approach for targeted drug delivery system, J. Colloid Interface Sci. 529 (2018) 415–425, https://doi.org/10.1016/j.jcis.2018.06.006.

[21] A. Sharma, A.D. Chougale, G. Salvan, P.B. Patil, Chapter 15. Magnetoresistance-based biosensors, in: M.H. Chaudhery (Ed.), Anal. Appl. Funct. Magn. Nanoparticles, Royal Society of Chemistry, Cambridge, 2021, pp. 369–396, https://doi.org/10.1039/9781839162756-00369.

[22] N.D.A.L. Miller, Dimercaptosuccinic acid (DMSA), a non-toxic, water-soluble treatment for heavy metal toxicity, Alternative Med. Rev. 3 (1998) 199–207.

[23] Y.J. Cha, M.J. Kim, Y.H. Choa, J. Kim, B. Nam, J. Lee, D.H. Kim, K.H. Kim, Synthesis and characterizations of surface-coated superparamagentic magnetite nanoparticles, IEEE Trans. Magn. 46 (2010) 443–446, https://doi.org/10.1109/TMAG.2009.2033205.

[24] Y.Q. Zhang, R. Dringen, C. Petters, W. Rastedt, J. Köser, J. Filser, S. Stolte, Toxicity of dimercaptosuccinate-coated and un-functionalized magnetic iron oxide nanoparticles towards aquatic organisms, Environ. Sci. Nano. 3 (2016) 754–767, https://doi.org/10.1039/c5en00222b.

[25] S. Sun, H. Zeng, D.B. Robinson, S. Raoux, P.M. Rice, S.X. Wang, G. Li, Monodisperse MFe_2O_4 (M = Fe, Co, Mn) nanoparticles, J. Am. Chem. Soc. 126 (2004) 273–279, https://doi.org/10.1021/ja0380852.

[26] Y. Waseda, E. Matsubara, K. Shinoda, X-Ray Diffraction Crystallography, Springer Berlin Heidelberg, Berlin, Heidelberg, 2011, https://doi.org/10.1007/978-3-642-16635-8.

[27] D. Maity, S. Choo, J. Yi, J.D. Ã, J.M.X. Ã, Synthesis of magnetite nanoparticles via a solvent-free thermal decomposition route, J. Magn. Magn Mater. 321 (2009) 1256–1259, https://doi.org/10.1016/j.jmmm.2008.11.013.

[28] L. Zhang, R. He, H.C. Gu, Oleic acid coating on the monodisperse magnetite nanoparticles, Appl. Surf. Sci. 253 (2006) 2611–2617, https://doi.org/10.1016/j.apsusc.2006.05.023.

[29] T.K.O. Vuong, D.L. Tran, T.L. Le, D.V. Pham, H.N. Pham, T.H. Le Ngo, H.M. Do, X. P. Nguyen, Synthesis of high-magnetization and monodisperse Fe_3O_4 nanoparticles via thermal decomposition, Mater. Chem. Phys. 163 (2015) 537–544, https://doi.org/10.1016/j.matchemphys.2015.08.010.

[30] H. Sharifi Dehsari, R.A. Harris, A.H. Ribeiro, W. Tremel, K. Asadi, Optimizing the binding energy of the surfactant to iron oxide yields truly monodisperse nanoparticles, Langmuir 34 (2018) 6582–6590, https://doi.org/10.1021/acs.langmuir.8b01337.

[31] Y. Jun, Y.-M. Huh, J. Choi, J.-H. Lee, H.-T. Song, S. Kim, S. Yoon, K.-S. Kim, J.-S. Shin, J.-S. Suh, J. Cheon, Nanoscale size effect of magnetic nanocrystals and their utilization for cancer diagnosis via magnetic resonance imaging, J. Am. Chem. Soc. 127 (2005) 5732–5733, https://doi.org/10.1021/ja0422155.

[32] S.I.C.J. Palma, M. Marciello, A. Carvalho, S. Veintemillas-Verdaguer, M.D. P. Morales, A.C.A. Roque, Effects of phase transfer ligands on monodisperse iron oxide magnetic nanoparticles, J. Colloid Interface Sci. 437 (2015) 147–155, https://doi.org/10.1016/j.jcis.2014.09.019.

[33] S. Zhang, X. Chen, C. Gu, Y. Zhang, J. Xu, Z. Bian, D. Yang, N. Gu, The effect of iron oxide magnetic nanoparticles on smooth muscle cells, Nanoscale Res. Lett. 4 (2009) 70–77, https://doi.org/10.1007/s11671-008-9204-7.

[34] S. Singh, K.C. Barick, D. Bahadur, Surface engineered magnetic nanoparticles for removal of toxic metal ions and bacterial pathogens, J. Hazard Mater. 192 (2011) 1539–1547, https://doi.org/10.1016/j.jhazmat.2011.06.074.

[35] R.P. Gupta, S.K. Sen, Calculation of multiplet structure of core p vacancy levels. II, Phys. Rev. B 12 (1975) 15–19. http://link.aps.org/doi/10.1103/PhysRevB.12.15.

[36] N.S. McIntyre, D.G. Zetaruk, X-ray photoelectron spectroscopic studies of iron oxides, Anal. Chem. 49 (1977) 1521–1529, https://doi.org/10.1021/ac50019a016.

[37] A.P. Grosvenor, B.A. Kobe, M.C. Biesinger, N.S. McIntyre, Investigation of multiplet splitting of Fe 2p XPS spectra and bonding in iron compounds, Surf. Interface Anal. 36 (2004) 1564–1574, https://doi.org/10.1002/sia.1984.

[38] P.M. Hallam, M. Gómez-Mingot, D.K. Kampouris, C.E. Banks, Facile synthetic fabrication of iron oxide particles and novel hydrogen superoxide supercapacitors, RSC Adv. 2 (2012) 6672–6679, https://doi.org/10.1039/c2ra01139e.

[39] B.J. Tan, K.J. Klabunde, P.M.A. Sherwood, X-ray photoelectron spectroscopy studies of solvated metal atom dispersed catalysts. Monometallic iron and bimetallic iron-cobalt particles on alumina, Chem. Mater. 2 (1990) 186–191, https://doi.org/10.1021/cm00008a021.

[40] O.F. Odio, L. Lartundo-Rojas, P. Santiago-Jacinto, R. Martínez, E. Reguera, Sorption of gold by naked and thiol-capped magnetite nanoparticles: an XPS approach, J. Phys. Chem. C 118 (2014) 2776–2791, https://doi.org/10.1021/jp409653t.

[41] M. Gogoi, P. Deb, G. Vasan, P. Keil, A. Kostka, A. Erbe, Direct monophasic replacement of fatty acid by DMSA on SPION surface, Appl. Surf. Sci. 258 (2012) 9685–9691, https://doi.org/10.1016/j.apsusc.2012.06.011.

[42] X. Guo, F. Mao, W. Wang, Y. Yang, Z. Bai, Sulfhydryl-modified Fe_3O_4@SiO_2 core/shell nanocomposite: synthesis and toxicity assessment in vitro, ACS Appl. Mater. Interfaces 7 (2015) 14983–14991, https://doi.org/10.1021/acsami.5b03873.

[43] L.S. Dake, D.R. Baer, J.M. Zachara, Auger parameter measurements of zinc compounds relevant to zinc transport in the environment, Surf. Interface Anal. 14 (1989) 71–75, https://doi.org/10.1002/sia.740140115.

[44] O. Selyshchev, Y. Havryliuk, M.Y. Valakh, V.O. Yukhymchuk, O. Raievska, O. L. Stroyuk, V. Dzhagan, D.R.T. Zahn, Raman and X-ray photoemission identification of colloidal metal sulfides as potential secondary phases in nanocrystalline Cu_2ZnSnS_4 photovoltaic absorbers, ACS Appl. Nano Mater. 3 (2020) 5706–5717, https://doi.org/10.1021/acsanm.0c00910.

[45] M. Sowa, D. Łastówka, A.I. Kukharenko, D.M. Korotin, E.Z. Kurmaev, S. O. Cholakh, W. Simka, Characterisation of anodic oxide films on zirconium formed in sulphuric acid: XPS and corrosion resistance investigations, J. Solid State Electrochem. 21 (2017) 203–210, https://doi.org/10.1007/s10008-016-3369-2.

[46] P. Guardia, B. Batlle-Brugal, A.G. Roca, O. Iglesias, M.P. Morales, C.J. Serna, A. Labarta, X. Batlle, Surfactant effects in magnetite nanoparticles of controlled size, J. Magn. Magn Mater. 316 (2007) 756–759, https://doi.org/10.1016/j.jmmm.2007.03.085.

[47] Q.A. Pankhurst, R.J. Pollard, Origin of the spin-canting anomaly in small ferrimagnetic particles, Phys. Rev. Lett. 67 (1991) 248–250, https://doi.org/10.1103/PhysRevLett.67.248.

[48] C.L. Warner, R.S. Addleman, A.D. Cinson, T.C. Droubay, M.H. Engelhard, M. A. Nash, W. Yantasee, M.G. Warner, High-performance, superparamagnetic, nanoparticle-based heavy metal sorbents for removal of contaminants from natural waters, ChemSusChem 3 (2010) 749–757, https://doi.org/10.1002/cssc.201000027.

[49] M. Qi, K. Zhang, S. Li, J. Wu, C. Pham-Huy, X. Diao, D. Xiao, H. He, Superparamagnetic Fe_3O_4 nanoparticles: synthesis by a solvothermal process and functionalization for a magnetic targeted curcumin delivery system, New J. Chem. 40 (2016) 4480–4491, https://doi.org/10.1039/c5nj02441b.

[50] V. Kumar, R.P. Singh, S. Kumar, A. Agarwal, P. Singh, Particle size determination and magnetic characterization of Fe_3O_4 nanoparticles using superconducting quantum interference device magnetometry, Sensor. Mater. 28 (2016) 191–199, https://doi.org/10.18494/SAM.2016.1169.

[51] L. Zhang, J. Guo, X. Huang, W. Wang, P. Sun, Y. Li, J. Han, Functionalized biochar-supported magnetic $MnFe_2O_4$ nanocomposite for the removal of Pb(II) and Cd(II), RSC Adv. 9 (2019) 365–376, https://doi.org/10.1039/c8ra09061k.

[52] F.P. Fato, D.W. Li, L.J. Zhao, K. Qiu, Y.T. Long, Simultaneous removal of multiple heavy metal ions from river water using ultrafine mesoporous magnetite nanoparticles, ACS Omega 4 (2019) 7543–7549, https://doi.org/10.1021/acsomega.9b00731.

[53] A. Afkhami, M. Saber-Tehrani, H. Bagheri, Simultaneous removal of heavy-metal ions in wastewater samples using nano-alumina modified with 2,4-dinitrophenylhydrazine, J. Hazard Mater. 181 (2010) 836–844, https://doi.org/10.1016/j.jhazmat.2010.05.089.

[54] N. Tang, C.-G. Niu, X.-T. Li, C. Liang, H. Guo, L.-S. Lin, C.-W. Zheng, G.-M. Zeng, Efficient removal of Cd^{2+} and Pb^{2+} from aqueous solution with amino- and thiol-functionalized activated carbon: isotherm and kinetics modeling, Sci. Total Environ. 635 (2018) 1331–1344, https://doi.org/10.1016/j.scitotenv.2018.04.236.

[55] V. Javanbakht, S.M. Ghoreishi, N. Habibi, M. Javanbakht, A novel magnetic chitosan/clinoptilolite/magnetite nanocomposite for highly efficient removal of Pb (II) ions from aqueous solution, Powder Technol. 302 (2016) 372–383, https://doi.org/10.1016/j.powtec.2016.08.069.

[56] H. Yuh-Shan, Citation review of Lagergren kinetic rate equation on adsorption reactions, Scientometrics 59 (2004) 171–177, https://doi.org/10.1023/B:SCIE.0000013305.99473.cf.

[57] Y.S. Ho, G. McKay, Pseudo-second order model for sorption processes, Process Biochem. 34 (1999) 451–465, https://doi.org/10.1016/S0032-9592(98)00112-5.

[58] T.K. Naiya, A.K. Bhattacharya, S.K. Das, Clarified sludge (basic oxygen furnace sludge) - an adsorbent for removal of Pb(II) from aqueous solutions - kinetics, thermodynamics and desorption studies, J. Hazard Mater. 170 (2009) 252–262, https://doi.org/10.1016/j.jhazmat.2009.04.103.

[59] U. Maheshwari, B. Mathesan, S. Gupta, Efficient adsorbent for simultaneous removal of Cu(II), Zn(II) and Cr(VI): kinetic, thermodynamics and mass transfer mechanism, Process Saf. Environ. Protect. 98 (2015) 198–210, https://doi.org/10.1016/j.psep.2015.07.010.

[60] I. Langmiur, The adsorption of gases on plane surfaces of glass, mica and platinum, J. Am. Chem. Soc. 60 (1918) 467–475, https://doi.org/10.1021/ja02242a004.

[61] X. Zhao, H. Wang, H. Peng, L. Wang, X. Lu, Y. Huang, J. Chen, T. Shao, Buoyant ALG/HA/HGMs composite adsorbents for highly efficient removal of copper from aqueous solution and contaminated kaolin soil, Chem. Eng. J. 327 (2017) 244–256, https://doi.org/10.1016/j.cej.2017.06.085.

[62] K.R. Hall, L.C. Eagleton, A. Acrivos, T. Vermeulen, Pore- and solid-diffusion kinetics in fixed-bed adsorption under constant-pattern conditions, Ind. Eng. Chem. Fundam. 5 (2002) 212–223, https://doi.org/10.1021/i160018a011.

[63] A.H. Chen, C.Y. Yang, C.Y. Chen, C.Y. Chen, C.W. Chen, The chemically crosslinked metal-complexed chitosans for comparative adsorptions of Cu(II), Zn(II), Ni(II) and Pb(II) ions in aqueous medium, J. Hazard Mater. 163 (2009) 1068–1075, https://doi.org/10.1016/j.jhazmat.2008.07.073.

[64] W. Qu, D. He, Y. Guo, Y. Tang, J. Shang, L. Zhou, R. Zhu, R.J. Song, Adsorption of Ni^{2+} and Pb^{2+} from water using diethylenetriamine-grafted Spirodela polyrhiza: behavior and mechanism studies, Environ. Sci. Pollut. Res. 26 (2019) 34562–34574, https://doi.org/10.1007/s11356-019-06558-0.

[65] T. Li, W. Zhang, S. Zhai, G. Gao, J. Ding, W. Zhang, Y. Liu, X. Zhao, B. Pan, L. Lv, Efficient removal of nickel(II) from high salinity wastewater by a novel PAA/ZIF-8/PVDF hybrid ultrafiltration membrane, Water Res. 143 (2018) 87–98, https://doi.org/10.1016/j.watres.2018.06.031.

[66] K. Chen, J. He, Y. Li, X. Cai, K. Zhang, T. Liu, Y. Hu, D. Lin, L. Kong, J. Liu, Removal of cadmium and lead ions from water by sulfonated magnetic nanoparticle adsorbents, J. Colloid Interface Sci. 494 (2017) 307–316, https://doi.org/10.1016/j.jcis.2017.01.082.

[67] S.B. Chen, Y.B. Ma, L. Chen, K. Xian, Adsorption of aqueous Cd^{2+}, Pb^{2+}, Cu^{2+} ions by nano-hydroxyapatite: single-and multi-metal competitive adsorption study, Geochem. J. 44 (2010) 233–239, https://doi.org/10.2343/geochemj.1.0065.

[68] I. Mobasherpour, E. Salahi, M. Pazouki, Comparative of the removal of Pb^{2+}, Cd^{2+} and Ni^{2+} by nano crystallite hydroxyapatite from aqueous solutions: adsorption isotherm study, Arab. J. Chem. 5 (2012) 439–446, https://doi.org/10.1016/j.arabjc.2010.12.022.

[69] A.V. Borhade, T.A. Kshirsagar, A.G. Dholi, J.A. Agashe, Removal of heavy metals Cd^{2+}, Pb^{2+}, and Ni^{2+} from aqueous solutions using synthesized azide cancrinite, $Na_8[AlSiO_4]_6(N_3)_{2.4}(H_2O)_{4.6}$, J. Chem. Eng. Data 60 (2015) 586–593, https://doi.org/10.1021/je500698x.

[70] J. Bayo, Kinetic studies for Cd(II) biosorption from treated urban effluents by native grapefruit biomass (Citrus paradisi L.): the competitive effect of Pb(II), Cu (II) and Ni(II), Chem. Eng. J. 191 (2012) 278–287, https://doi.org/10.1016/j.cej.2012.03.016.

[71] A.Z.M. Badruddoza, Z.B.Z. Shawon, W.J.D. Tay, K. Hidajat, M.S. Uddin, Fe_3O_4/cyclodextrin polymer nanocomposites for selective heavy metals removal from industrial wastewater, Carbohydr. Polym. 91 (2013) 322–332, https://doi.org/10.1016/j.carbpol.2012.08.030.

[72] X. Guo, B. Du, Q. Wei, J. Yang, L. Hu, L. Yan, W. Xu, Synthesis of amino functionalized magnetic graphenes composite material and its application to remove Cr(VI), Pb(II), Hg(II), Cd(II) and Ni(II) from contaminated water, J. Hazard Mater. 278 (2014) 211–220, https://doi.org/10.1016/j.jhazmat.2014.05.075.

[73] A. Heidari, H. Younesi, Z. Mehraban, Removal of Ni(II), Cd(II), and Pb(II) from a ternary aqueous solution by amino functionalized mesoporous and nano mesoporous silica, Chem. Eng. J. 153 (2009) 70–79, https://doi.org/10.1016/j.cej.2009.06.016.

[74] M. Shafiee, R. Foroutan, K. Fouladi, M. Ahmadlouydarab, B. Ramavandi, S. Sahebi, Application of oak powder/Fe_3O_4 magnetic composite in toxic metals removal from aqueous solutions, Adv. Powder Technol. 30 (2019) 544–554, https://doi.org/10.1016/j.apt.2018.12.006.

[75] D.F. Enache, E. Vasile, C.M. Simonescu, A. Răzvan, A. Nicolescu, A.-C. Nechifor, O. Oprea, R.-E. Pătescu, C. Onose, F. Dumitru, Cysteine-functionalized silica-coated magnetite nanoparticles as potential nanoadsorbents, J. Solid State Chem. 253 (2017) 318–328, https://doi.org/10.1016/j.jssc.2017.06.013.

[76] Y. Tan, M. Chen, Y. Hao, High efficient removal of Pb(II) by amino-functionalized Fe_3O_4 magnetic nano-particles, Chem. Eng. J. 191 (2012) 104–111, https://doi.org/10.1016/j.cej.2012.02.075.

[77] D. Singh, S.K. Singh, N. Atar, V. Krishna, Amino acid functionalized magnetic nanoparticles for removal of Ni(II) from aqueous solution, J. Taiwan Inst. Chem. Eng. 67 (2016) 148–160, https://doi.org/10.1016/j.jtice.2016.06.017.

[78] M. Adeli, Y. Yamini, M. Faraji, Removal of copper, nickel and zinc by sodium dodecyl sulphate coated magnetite nanoparticles from water and wastewater samples, Arab. J. Chem. 10 (2017), https://doi.org/10.1016/j.arabjc.2012.10.012. S514–S521.

[79] S. Venkateswarlu, S. Himagirish Kumar, N.V.V. Jyothi, Rapid removal of Ni(II) from aqueous solution using 3-Mercaptopropionic acid functionalized bio magnetite nanoparticles, Water Resour. Ind. 12 (2015) 1–7, https://doi.org/10.1016/j.wri.2015.09.001.

[80] S. Ghafoor, S. Ata, Synthesis of carboxyl-modified Fe_3O_4@SiO_2 nanoparticles and their utilization for the remediation of cadmium and nickel from aqueous solution, J. Chil. Chem. Soc. 62 (2017) 3588–3592, https://doi.org/10.4067/s0717-97072017000303588.

[81] J. Gong, L. Chen, G. Zeng, F. Long, J. Deng, Q. Niu, X. He, Shellac-coated iron oxide nanoparticles for removal of cadmium(II) ions from aqueous solution, J. Environ. Sci. (China) 24 (2012) 1165–1173, https://doi.org/10.1016/S1001-0742(11)60934-0.

[82] H.L. Fan, S.F. Zhou, W.Z. Jiao, G.S. Qi, Y.Z. Liu, Removal of heavy metal ions by magnetic chitosan nanoparticles prepared continuously via high-gravity reactive precipitation method, Carbohydr. Polym. 174 (2017) 1192–1200, https://doi.org/10.1016/j.carbpol.2017.07.050.